River Flow Induced Nonlinear Modulation of M_4 Overtide in Large Estuaries

Guo, Leicheng; Zhu, Chunyan; Cai, Huayang; Wang, Zheng Bing; Townend, Ian; He, Qing

DOI
10.1007/s12237-023-01183-0

Publication date
2023

Document Version
Final published version

Published in
Estuaries and Coasts

Estuaries and Coasts
https://doi.org/10.1007/s12237-023-01183-0

River Flow Induced Nonlinear Modulation of M_4 Overtide in Large Estuaries

Leicheng Guo[1] · Chunyan Zhu[1] · Huayang Cai[2] · Zheng Bing Wang[3,4] · Ian Townend[5] · Qing He[1]

Received: 30 June 2022 / Revised: 1 February 2023 / Accepted: 1 February 2023

Abstract

River discharge is known to enhance tidal damping and tidal wave deformation in estuaries. While the damping effect on astronomical tides has been well documented, river impact on tidal wave deformation and associated overtide generation (shallow water harmonics of one or more astronomical constituents, such as M_4) remains insufficiently understood. Overtides affect tidal asymmetry, extreme water levels, and subsequent sediment transport and flooding management, thus meriting in-depth examination. Being inspired by unusual overtide changes in the landward and seaward parts of the Changjiang Estuary under low and high river discharges, in this work, we use a schematized tidal estuary model to systematically explore overtide variations under different river discharges. Model results show enhanced overtide generation in the case with river discharge compared with that without river impact. The M_4 amplitude decreases in the landward parts of the estuary, but increases in the seaward parts under increasing river discharges. The potential energy of M_4 integrated throughout the estuary shows nonlinear variations and reaches a transitional maximum when the river discharge to tidal mean discharge (R2T) ratio at the mouth is close to unity. Similar nonlinear behaviors are observed for compound tides like MS_4 when more astronomical constituents are prescribed and triad tidal interactions are enabled. The space-dependent overtide variability is more profound in large estuaries with high river discharges like the Amazon and Changjiang estuaries. It is ascribed to the inherently nonlinear river-tide interactions, specifically the twofold effects of river discharge in enhancing bottom stress, which simultaneously enhances dissipation of astronomical constituents and reinforces the energy transfer to overtides. These findings highlight the profound nonlinear impact of river discharge on overtides, and inform the study of tidal asymmetry and compound flood risk in large estuaries and deltas.

Keywords Estuary · Overtide · Bottom stress · River discharge

Introduction

Tidal Propagation

Tides are a primary force driving water level oscillations, horizontal water motion, and transport of sediment and contaminant in estuarine and coastal environments. Examination of tidal wave dynamics supports many aspects of coastal management, including flooding risk mitigation, coastal erosion defense, and wetland conservation.

Tidal dynamics in oceanic and coastal waters have been extensively studied for centuries (Green 1837; Talke and Jay 2020). It is well established that tidal waves traveling into estuaries are altered in amplitude and wave shape due to water depth changes, channel convergence (Jay 1991; Friedrichs and Aubrey 1994; Lanzoni and Seminara 1998; Talke and Jay 2020), and river discharge (Godin 1985; Horrevoets et al. 2004; Cai et al. 2014). It is also well known that river flow enhances tidal energy dissipation and tidal damping by enhancing the bottom friction (Jay and Flinchem 1997; Godin 1999; Horrevoets et al. 2004; Toffolon and Savenije 2011).

Tides are also distorted inside estuaries. Tidal distortion is ascribed to the fact that high water travels faster than low water, owing to larger water depth and tidal wave celerity during high water. This results in shorter rising

Communicated by Arnoldo Valle-Levinson

Key points
1. River discharge enhances tidal wave deformation and induces larger overtides in estuaries.
2. Overtide generation is maximal when the river discharge to tidal mean discharge ratio is close to unity.
3. The quadratic bottom stress plays a dominant role in controlling the space-dependent overtide variations.

✉ Leicheng Guo
lcguo@sklec.ecnu.edu.cn

Extended author information available on the last page of the article

tide and longer falling tide, i.e., tidal wave deformation, which is a result of interactions between M_2 and its overtide M_4 (Pugh 1987). The amplitude of M_4 overtide is small and insignificant in relatively deep and open coastal seas, but can become profound inside shallow water environments. Generation of M_4 tide has been examined in tide-dominant estuaries and inlets given that the resultant tidal asymmetry controls tide-averaged sediment transport and morphological changes (Parker 1984; Speer and Aubrey 1985; Friedrichs and Aubrey 1988; Le Provost 1991; Walters and Werner, 1991; etc.). Furthermore, river flow reinforces tidal wave deformation by prolonging falling tides and shortening rising tides (Stronach and Murty 1989; Gallo and Vinzon 2005). This increased wave distortion is apparent from larger M_4 to M_2 amplitude ratios.

A small number of studies, however, suggest that the impact of river flow on tidal wave deformation and overtide generation exhibits more variability. Godin (1985, 1999) reported accelerated low water and retarded high water in the upper Saint Lawrence Estuary under larger river discharge, whereas the high water was hastened and the low water was delayed in the seaward parts of the estuary. In the Changjiang Estuary, the amplitude of the quarter-diurnal tidal specie (the tidal constituents with four cycles a day, including M_4, MS_4, and MN_4), resolved by continuous wavelet transform method, becomes larger in the seaward parts of the estuary, but smaller in the landward parts under higher river discharges (Guo et al. 2015, 2019). These studies imply that the M_4 overtide is sensitive to river discharge magnitude and it displays space-dependent variations under different river discharges.

The locally generated overtide is related to the nonlinear dynamics in shallow waters, which stimulate energy transfer from astronomical constituents to overtides (Parker 1984; Talke and Jay 2020). Nonlinearity enters the mathematical representation of a tidal system through the divergence of excess volume in the continuity equation and the advection and bottom friction terms in the momentum equation (Speer and Aubrey 1985; Parker 1984, 1991; Wang et al. 1999, 2002; Losada et al. 2017). Pioneering studies with scaling analysis suggested that the advection term is insignificant when scaled with estuarine length or wavelength in short and tide-dominated estuaries, thus was ignored in analytical solutions (Speer and Aubrey 1985; Friedrichs and Aubrey 1994).

In the presence of a river flow, the advection term may play a role in slowing down incident tidal waves and speeding up the reflected waves (Godin 1985, 1991; van Rijn 2011; Kästner et al. 2019). This is because river flow enlarges the mean current velocities; therefore the advection term becomes significant (Talke and Jay 2020). Gallo and Vinzon (2005) and Losada et al. (2017) evaluated the relative importance of the nonlinear terms on overtide generation in the case of the Amazon and Guadalquiver Estuaries, respectively. The quadratic bottom stress was found to play a dominant role in reducing tidal amplitudes and decreasing wave celerity (Proudman 1953; Godin 1985; Le Provost 1991; Horrevoets et al. 2004), and stimulating the generation of new harmonics (Proudman 1953; Pingree and Maddock 1978; Parker 1984; Wang et al. 1999; Gallo and Vinzon 2005).

Inspirations from the Changjiang Estuary

In the case of the Changjiang Estuary, preliminary analysis of tidal water level data suggests peculiar overtide changes under low and high river discharges. The Changjiang Estuary is the second longest estuary in the world, with a tide-influenced river reach as along as 650 km (Fig. 1a), only after the ~1100 km tidal penetration in the Amazon Estuary (Gallo and Vinzon 2005). River discharge at the limit of tidal wave propagation, Datong gauge, varies seasonally in the range of 10,000–60,000 m^3/s (Fig. 1b; Guo et al. 2018). The incident astronomical tides are semi-diurnal with a maximum tidal range of 5.9 m, and the M_2 is the most significant constituent, followed by S_2, O_1, and K_1. The incoming tidal waves are firstly amplified before traveling into the estuary, owing to a landward decrease in water depth (Fig. 1c). Tidal waves are then predominantly dissipated inside the estuary despite width convergence in the seaward parts of the estuary, because of stronger influence of bottom friction and river discharge. Tidal damping is more significant in the wet seasons when river discharge is higher, particularly in the landward parts of the estuary upstream of Jiangyin.

Significant M_4 overtide is detected inside the Changjiang Estuary, while it is insignificant in the coastal waters (Fig. 1d). In addition, the M_4 amplitude is overall larger in the seaward parts of the estuary in the wet seasons when the river discharge is higher (Fig. 1d). The amplitude ratios of the quarter- to semi-diurnal tidal species (resolved by continuous wavelet transform) decrease with increasing river discharge in the landward parts of the estuary, but increase in the seaward parts (Fig. 1e; Guo et al. 2015). Furthermore, the skewness of the time derivative of tidal water levels, which indicates the duration asymmetry between rising tide and falling tides (Nidzieko 2010), is predominantly positive, suggesting shorter rising tide. The positive skewness is larger under higher river discharge at the seaward gauge, but reduces at the landward gauge. It suggests increased falling tide duration (compared with rising tide duration) in the seaward parts of the estuary but decreased in the landward parts when river discharge increases (Fig. 1f; Guo et al. 2019).

These preliminary results (Fig. 1d–f) consistently demonstrate that the overtides display distinctive variations between

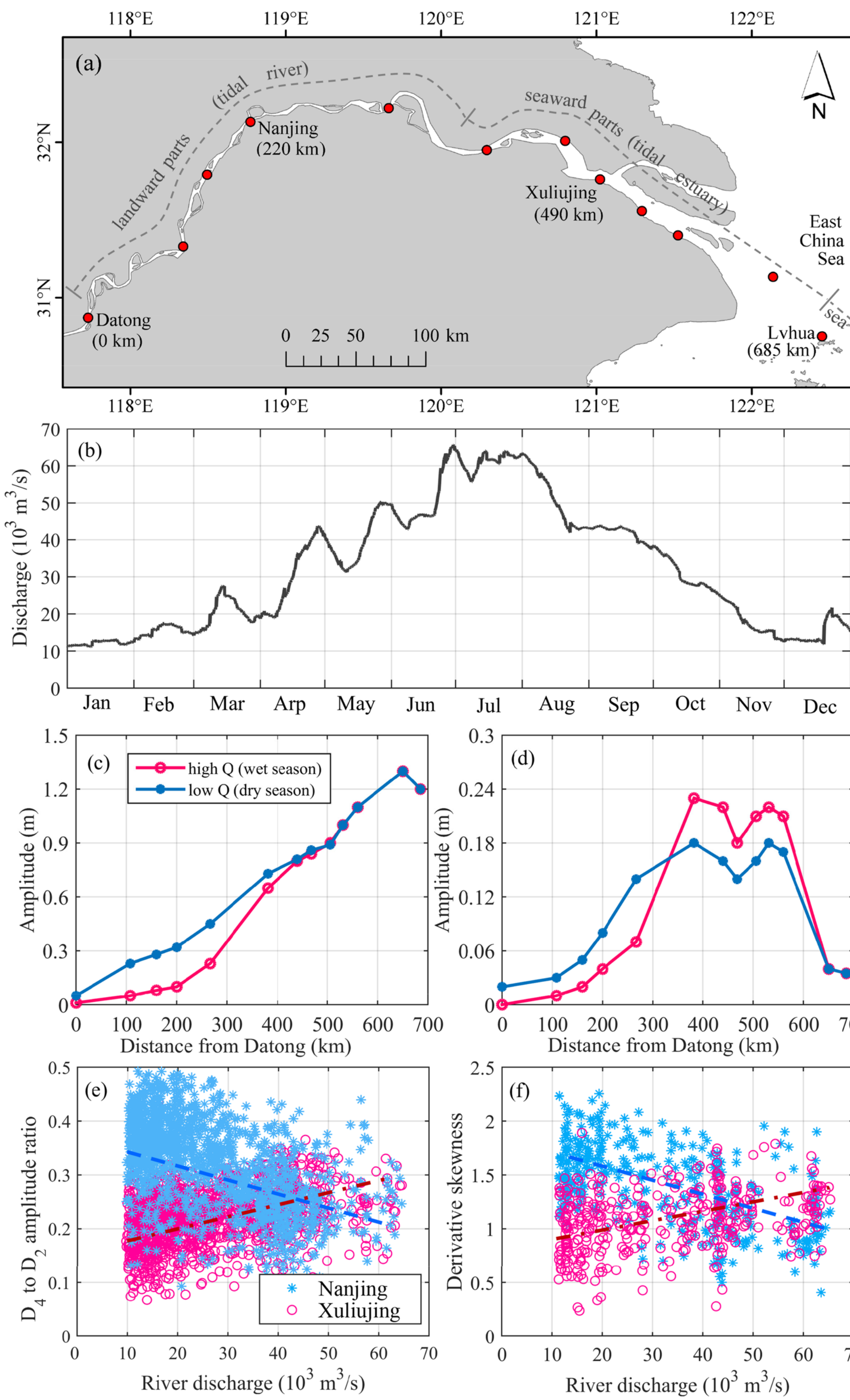

Fig. 1 **a** The geometry and tidal gauges in the Changjiang Estuary, **b** river discharge variations within a year course, along-river **c** M_2, and **d** M_4 amplitude variations in the dry and wet seasons, **e** amplitude ratios of the quarter-diurnal to semi-diurnal tides, and **f** skewness of the time derivative of tidal water levels at Nanjing and Xuliujing. Details of the Changjiang Estuary and the tidal data are given in Guo et al. (2015). The numbers in the brackets in panel **a** indicate the seaward distance from Datong. The data in panels **c**–**e** is from Guo et al. (2016) and that in panel **f** is from Guo et al. (2019)

the landward and seaward parts of the estuary in response to low and high river discharges. This provides a clear indication of the spatial variability in large estuaries. However, understanding of the spatial overtide variations under a wider range of river discharges and the physical controls is incomplete.

Rationale and Objective

Examination of tidal data has provided a basic framework for our understanding of tidal dynamics in estuaries (Dronkers 1964; Godin 1985). One challenge in tidal data analysis lies in that river discharges can vary in a large range in short periods, thus inducing strong non-stationary variations in tidal dynamics. Conventional harmonic analysis, adopting a stationary assumption, may not accurately resolve the non-stationary river tides (Jay and Flinchem, 1997), although there have been attempts to use continuous wavelet transform (Jay et al. 2014; Guo et al. 2015) and a complex demodulation method (Bloomfield 2013) as complementary approaches.

In addition, analytical solutions of tidal dynamic equations, which drop the advection term or adopt a linear assumption or a simplified expansion of the friction term (Green 1837; Kreiss 1957; Jay 1991; Parker 1991; Friedrichs and Aubrey 1994; van Rijn 2011), have facilitated exanimation of leading-order wave propagation such as landward damping and amplification of astronomical tides (Jay 1991; Friedrichs and Aubrey 1994; Lanzoni and Seminara 1998; Savenije 2005). More recent improvements to these analytical methods take into account more than one tidal component, use a robust approximation of the nonlinear friction term, and include their impact on morphodynamic changes (Lanzoni and Seminara 1998; Ridderinkhof et al. 2014; Alebregtse and de Swart 2016; Chernetsky et al. 2010; Dijkstra et al. 2017).

Numerical simulations of tidal dynamics provide an alternative approach that can fully capture the nonlinear dynamics without simplification. They include the detailed changes in estuarine geometry and are widely employed to examine tides in estuaries with more complexity in morphology and dynamics (Lu et al. 2015; Elahi et al. 2020). To cope with the strong nonlinearity in tidal dynamics in long estuaries with highly varying river discharges, in this work, we aim to combine the advantages of these methods by using a numerical model of a schematized estuary. The objectives of this study are to explore (1) how overtides change under different river discharges and nonlinear river-tide interactions, and (2) what is the controlling impact of river flow and nonlinear processes on the spatial variability of overtide.

Methodology

Theoretical Analysis of Overtide Generation

Tidal wave propagation in a 1D model is governed by the width-averaged shallow water equations, i.e., the continuity and momentum conservation equations, when the effect of Coriolis force and density variations is neglected (Dronkers 1964), as follows,

$$\frac{\partial \eta}{\partial t} + \frac{\partial u(h+\eta)}{\partial x} = 0 \tag{1}$$

$$\frac{\partial u}{\partial t} + \frac{\partial u}{\partial x} + g\frac{\partial \eta}{\partial x} + \frac{gu|u|}{C^2(h+\eta)} = 0 \tag{2}$$

where u is velocity, η is water height above mean sea level, h is water depth below mean sea level, g is gravitational acceleration (9.8 m^2/s), and C is a Cheźy friction coefficient prescribed as 65 $m^{1/2}/s$ uniformly, which leads to predominantly landward tidal damping within the schematized estuary, as that observed in reality (see Figs. 1 and 3).

In the presence of a river discharge, the water level height is composed of a mean water height related to river flow η_0, and a tide-induced water level oscillation,

$$\eta(x,t) = \eta_0(x) + \eta_{M2}(x)\cos(\omega t - kx) \tag{3}$$

in case of the presence of M_2 tide only, in which η_{M2} is the surface amplitude of M_2, and ω is the frequency of M_2, and k is tidal wave number. Similarly, the current is composed of a mean current and a tidal component,

$$u(x,t) = -u_0(x) + u_{M2}(x)\cos(\omega t - kx - \theta) \tag{4}$$

in which u_0 is the mean current velocity while the minus sign indicates the seaward direction, u_{M2} is the velocity amplitude of M_2, and θ is the phase difference between tidal surface wave and tidal currents. Overtide components are not included in Eqs. (3) and (4) as a simplification, which will not fundamentally change the following analytical description in identifying their internal generation.

Three nonlinear terms are identified in the tidal wave equations, namely the discharge gradient term in the continuity equation, and the advection and quadratic friction terms in the momentum equation:

$$\text{Discharge gradient}: \frac{\partial u(h+\eta)}{\partial x} = \frac{\partial (uh)}{\partial x} + \frac{\partial (u\eta)}{\partial x} \tag{5}$$

$$\text{Advection}: u\frac{\partial u}{\partial x} = \frac{\partial}{\partial x}\left(\frac{u^2}{2}\right) \tag{6}$$

$$\text{Bottom friction}: \frac{gu|u|}{C^2(h+\eta)} \approx \frac{g}{C^2}\left(\frac{u|u|}{h} - \frac{\eta u|u|}{h^2}\right) \tag{7}$$

The bottom friction term is approximately expanded into a bottom shear stress term and a term considering depth variations, as the two terms on the right hand of Eq. (7), respectively, according to Godin and Martinez (1994), given the tidal amplitude to water depth ratio ($|\eta|/h$) is generally smaller than one. Note that the bottom friction term can be calculated accurately with resolved water depths and velocities in the numerical model, while the approximation of Eq. (7) is just used to analytically demonstrate how the friction would lead to local generation of compound tides and overtides. Firstly, considering a situation when river discharge is small and the associated mean current (u_0) is insignificant, the quadratic bottom stress can be further expressed by Fourier decomposition according to Le Provost (1991) and Wang et al. (1999):

$$\frac{u|u|}{h} \approx \frac{u_{M2}^2}{h} \sum_{n=0,1,2,\ldots} (-1)^{n+1} \frac{8}{(2n-1)(2n+1)(2n+3)\pi} \cos[(2n+1)\omega t]\cos(nkx) \tag{8}$$

Equation (8) suggests that the self-interaction of M_2 tide through the quadratic bottom stress produces a series of overtide harmonics with odd-multiple frequencies, e.g., M_6 and M_{10} (Parker 1984). In addition, Eq. (8) also yields a contribution to the same frequency as M_2 (when $n=0$), which suggests tidal energy dissipation via the quadratic shear stress term (Wang et al. 1999). Similarly, the depth variation term in Eq. 7 can be expressed as:

$$\frac{\eta u|u|}{h^2} \approx \frac{\eta_{M2} u_{M2}^2}{h^2} \sum_{n=0,1,2,\ldots} (\ldots)\cos(\omega t)\cos[(2n+1)\omega t]$$

$$= \frac{\eta_{M2} u_{M2}^2}{h^2} \sum_{n=0,1,2,\ldots} (\ldots)[\frac{1}{2}\cos(2n\omega t) + \frac{1}{2}\cos(2n+2)\omega t] \tag{9}$$

Equation (9) suggests that self-interaction of M_2 tide through the depth variation term generates even-multiple frequency harmonics, e.g., M_4 and M_8. Similar decomposition analysis for the advection and discharge gradient term suggests the generation of even-frequency overtide as well (Parker 1984; Wang et al. 1999). Following similar logic, when two components such as M_2 and S_2 tides are prescribed, compound tides with frequencies the sums (e.g., MS_4) or differences (e.g., MSf) of the prescribed constituents are generated. The focus of this study is devoted to M_4 overtide, given it is the first overtide of M_2 and of profound importance for study of tidal asymmetry.

To further explore the controlling mechanisms of overtide generation, we adopt the approximation of the quadratic bottom stress according to Godin and Martinez (1994) and Godin (1999), as follows,

$$u|u| \approx 0.35u + 0.71u^3 \tag{10}$$

Replacing Eqs. (3) and (4) with Eq. (10) and using the sine and cosine summation rules, the harmonic decomposition approach of the nonlinear terms is used to identify their relative importance on the M_4 overtide. Following the methods in Gallo and Vinzon (2005) and Lieberthal et al. (2019) but considering both quadratic bed shear and depth variation terms, we can identify the contribution of the three nonlinear terms on M_4 overtide generation, i.e., discharge gradient, advection, and bottom friction, based on the modeled mean water height, mean current, and surface wave amplitudes and velocity amplitudes of M_2 and M_4 tides,

$$\text{Discharge gradient}: 0.5u_{M2}d\eta_{M2}/dx + 0.5\eta_{M2}du_{M2}/dx \tag{11}$$

$$\text{Advection}: 0.5u_{M2}du_{M2}/dx \tag{12}$$

$$\text{Friction}: \frac{1.065g}{C^2h}u_0u_{M2}^2 + \frac{g}{C^2h^2}[1.065\eta_0u_0u_{M2}^2 + 0.525u_0^2\eta_{M2}u_{M2} + 0.355\eta_{M2}u_{M2}^3] \tag{13}$$

The first term in Eq. (13) is ascribed to the quadratic bottom shear while the other terms are attributed to the depth variations. The advection and friction terms are normalized by squared maximum velocity and the discharge gradient term is normalized by the product of maximum velocity and maximum water level range. Equations (11) to (13) indicate that the interaction between the mean current and M_2 velocity would generate even-frequency harmonics like M_4 via both the quadratic bed shear stress and depth variation terms, which suggests river-enhanced M_4 overtide generation.

Given strong spatial variations in M_4 amplitude, we further integrate the total potential M_4 energy along the estuary (van Rijn 2011), as follows:

$$\int_0^L 0.5\rho g b(x)A(x)^2 dx/L \tag{14}$$

where L is the channel length, ρ is the water density, b is channel width, and A is the amplitude of M_4 tide which varies along the estuary. The integrated energy hence indicates the overall strength of overtide throughout the estuary under different river discharges.

Numerical Model Setup

In this study, we seek to capture the nonlinear tidal dynamics by using a numerical model, i.e., the open-source Delft3D codes, which have been widely validated and used in varying estuarine and coastal environments (Lesser et al. 2004). We construct a schematized 1D estuary model, which is 650 km long and is composed of a weakly convergent upstream segment (km-0 to km-400, width varying from 2 to 5 km) and a strongly convergent downstream segment (km-400 to km-650, width varying from 5 to 32 km (Fig. 2a). This convergent planform mimics the Changjiang Estuary, although excluding the regional width changes, and the geometry is used as a reference case.

Channel convergence is expected to affect tidal wave propagation and wave deformation (Jay 1991; van Rijn 2011; Talke and Jay 2020). To further explore the impact of basin geometry, we set up a prismatic channel model with similar

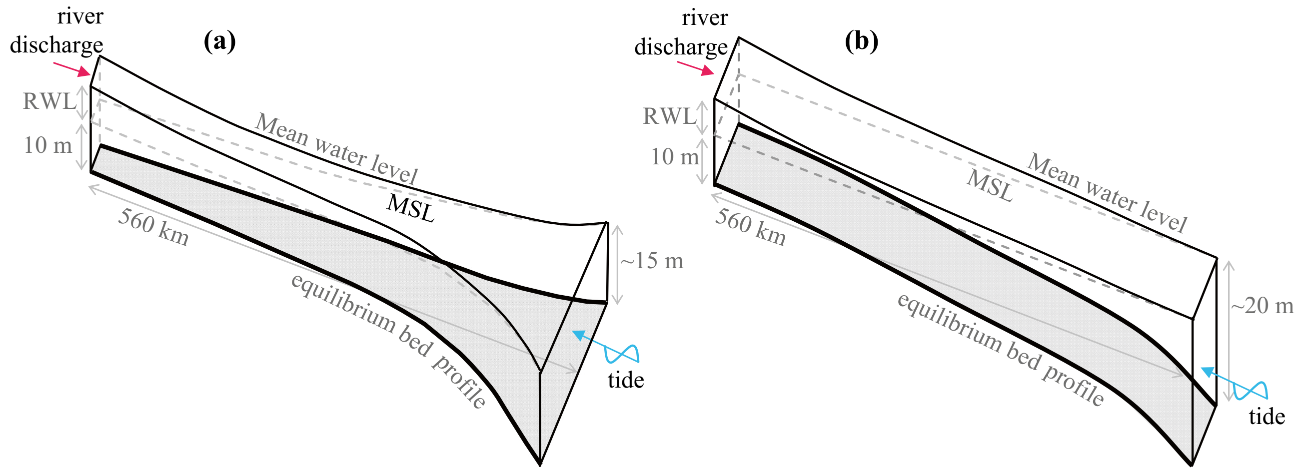

Fig. 2 Sketches of the schematized estuary model outline and settings considering **a** a convergent and **b** a prismatic planform. The shade face indicates the equilibrium bed profile. The RWL and MSL indicate residual water level and mean sea level, respectively

settings as the convergent estuary (i.e., 2 km width and similar length; Fig. 2b). Moreover, we configure similar estuaries with varying convergence rates, i.e., with a convergence length of 600 km, 300 km, and 150 km (Figure S1 and Table 1). The width convergence rate, defined as the ratio of the convergence length to the physical estuary length, varies in the range of 0.23–0.92, which is representative of the convergence rate of the estuaries in the real world (Lanzoni and D'Alpaos 2015).

The model is forced by river discharge and tides. For simplicity, we mainly consider a semi-diurnal M_2 constituent with an amplitude of 1.0 m at first, and then run extra sensitivity simulations considering different M_2 amplitudes (2.0 m and 0.5 m) and the situation with both M_2 (an amplitude 1.0 m) and S_2 (0.5 m) to facilitate more tidal interactions and generation of compound tide like MS_4 (Table 1). Other astronomical constituents like O_1 and K_1 are excluded because they would not affect the M_2 propagation very much.

River discharge is prescribed by constant values of 0, 10,000, 30,000, and 60,000 m^3/s, symbolized as Q0, Q1, Q3, and Q6 scenarios, respectively, to facilitate harmonic analysis with a stationary assumption. A dimensionless parameter, defined as the ratio of river discharge to tide-averaged mean discharge (i.e., tidal prism divided by tidal period) at the mouth section (R2T ratio), is estimated to be 0, 0.5, 2.6, and 42, respectively, in the prismatic channel forced by a M_2 tide 1.0 m in amplitude. The four situations thus can be classified into tide-dominant, low, medium, and very high river discharge circumstances, respectively (see the "Quantification of the River Discharge Threshold" section). As the river discharge is prescribed constant, harmonic analysis is applicable to the modeled time series of water levels and currents (Pawlowicz et al. 2002), which outputs mean water height, mean current, and the amplitudes and phases of surface wave and velocity of M_2 and M_4 constituents for further analysis.

Table 1 Model setting and sensitivity simulations. A indicates the tidal amplitude and L_b is the convergence length. Q indicates river discharge, and R2T is the river discharge to tidal discharge ratio at the mouth section under a M_2 tide with 1.0 m amplitude. L_b is the width convergence length in the depiction of width variations $B = B_0\exp(-x/L_b)$

Geometry	Boundary conditions			Name
	Tidal forcing	Q (m^3/s)	R2T	
Width variations mimicking the Changjiang Estuary	M_2 tide ($A = 1.0$ m)	0	0	cQ0
		10,000	0.2	cQ1
		30,000	0.75	cQ3
		60,000	2.1	cQ6
Prismatic channel	M_2 tide ($A = 1.0$ m)	0	0	pQ0
	M_2 tide ($A = 0.5$, 2.0 m)	10,000	0.5	pQ1
	M_2 tide ($A = 1.0$ m) + S_2 tide ($A = 0.5$ m)	30,000	2.6	pQ3
		60,000	42	pQ6
Smaller convergence rate, $L_b = 600$ km	M_2 tide ($A = 1.0$ m)	0–60,000*	0–2.5	SCs
Medium convergence rate, $L_b = 300$ km	M_2 tide ($A = 1.0$ m)	0–60,000*	0–1.63	MCs
Large convergence rate, $L_b = 150$ km	M_2 tide ($A = 1.0$ m)	0–60,000*	0–1.54	LCs

*indicates that river discharge are prescribed by values in the range of 0–60,000 m^3/s with an increment of 5000 m^3/s

To obtain a suitable bottom profile for the tidal model, we first run a morphodynamic simulation based on the above-mentioned model outline, with an M_2 tide and a river discharge seasonally varying between 10,000 and 60,000 m^3/s as the boundary forcing conditions, as presented in Guo et al. (2016). The long-term morphodynamic simulation starts from an initial sloping bed with depth varying from 5 to 15 m seaward, considers sediment transport and bed level changes, which leads to a dynamic morphological equilibrium when bed level change rates have significantly slowed down at the centennial time scales (Guo et al. 2016). The eventual equilibrium bed profile is then used as the bottom level condition in the tidal simulations. Similar morphodynamic simulations are conducted to obtain close-to-equilibrium bed profiles used in the sensitivity scenarios. An equilibrium bed profile is used in the tidal simulations to maintain consistency between the boundary forcing conditions (river discharge and tides) and the morphology (width and depth). Based on this equilibrium bed profile and given high river discharge imposed, the incoming tides are largely dissipated in the landward parts of the estuary; thus, the influence of wave reflection is minimized.

Past studies using similar 1D representation of tidal estuaries confirm the capture of leading-order dynamic processes (Friedrichs and Aubrey 1994; Lanzoni and Seminara 1998). Nevertheless, it is noteworthy that the 1D model excludes tidal flats and assumes uniform water density. These excluded processes may lead to additional momentum loss, reduction in bottom drag, and then influence tidal asymmetry (Friedrichs and Aubrey 1988; Talke and Jay 2020). Although simplified, the model provides a virtual lab where tidal wave propagation, deformation and associated overtide dynamics under varying river discharges can be straightforwardly isolated from the influences of basin geometry and irregular shoreline, which enables exploration of river-tide interactions and overtides.

Model Results

Tidal Variations Under Varying River Discharges

The streamwise variations of tidal amplitudes for both astronomical constituent and overtide in the reference case are shown in Fig. 3. The M_2 tide is slightly amplified in the seaward regions close to the mouth, owing to channel convergence (Fig. 3a). Landward of that, the M_2 tide is predominantly dissipated, and river discharge enhances the damping in the landward direction.

In addition, a considerable M_4 tide is detected in the cQ0 scenario (no river discharge) with a local amplitude maximum around km-450 (Fig. 3b). The M_4 amplitude becomes larger throughout the estuary in the cQ1 scenario compared with that in cQ0 (Fig. 3b). However, under further higher river discharges, the M_4 amplitude reduces in the landward parts of the estuary, e.g., landward km-300, but continues to increase in the seaward parts, e.g., seaward km-500 (Fig. 3b). The location with maximal M_4 amplitude moves slightly landward as the river discharge increases from zero (i.e., from km-450 in the cQ0 scenario to km-400 in the cQ1 scenario), but seaward as the river discharge further increases (i.e., from km-420 in the cQ3 scenario to km-500 in the cQ6 scenario).

The M_4 to M_2 amplitude ratio exhibits similar variations as the M_4 amplitude, but the ratio is overall larger in

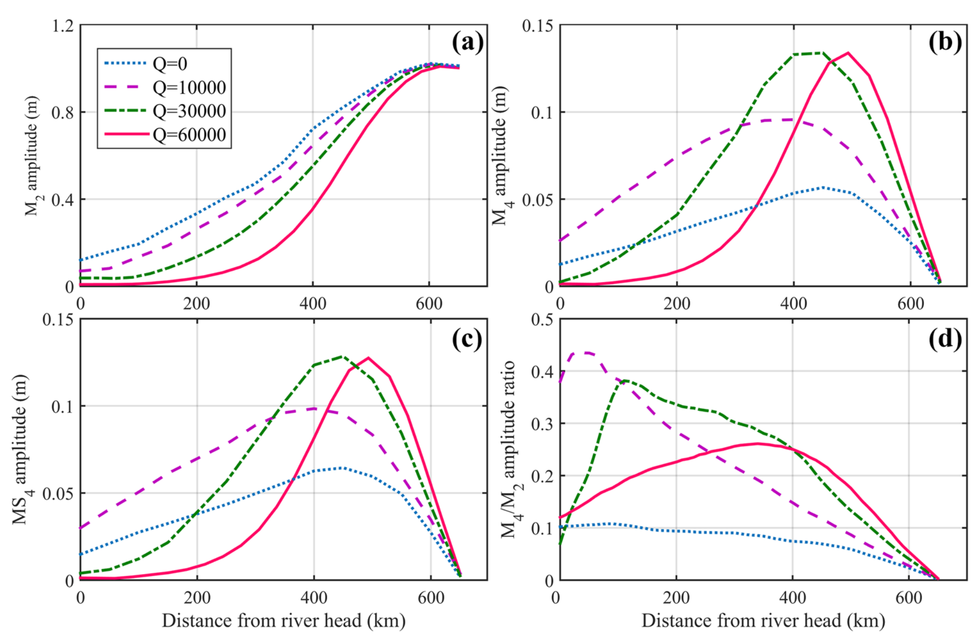

Fig. 3 The model-reproduced longitudinal variations of **a** M_2 amplitude, **b** M_4 amplitude, **c** MS_4 amplitude (in the scenario when both M_2 and S_2 are imposed at the boundary), and **d** the M_4 to M_2 amplitude ratios in the reference convergent estuary

the landward parts of the estuary where the amplitudes of both M_2 and M_4 tides are small (Fig. 3d). The increasingly damped and distorted tidal waves further illustrate the river impact on the incoming tides (see Figure S2 in the SI).

A compound constituent MS_4 is generated and detected inside the estuary when both M_2 and S_2 tides are imposed at the seaward boundary of the model. The MS_4 tide exhibits similar spatial variations as M_4 tide in response to increased river discharges (Fig. 3c). Similar results can be obtained for other overtides (e.g., M_6, MN_4, and S_4) if more astronomical constituents are prescribed and associated tidal interactions activated. We therefore focus on the M_4 overtide for the presentation of other results.

Sensitivity to Channel Convergence

In the prismatic estuary, river discharge substantially elevates the mean water levels (Fig. 4a). The incoming M_2 tide is persistently damped inside the estuary, without any amplification (Fig. 4b). Larger river discharges elevate the mean water level more and increase the streamwise water level gradients, leading to more dissipation of the astronomical tides.

Significant M_4 overtide is detected inside the estuary, although its amplitude is overall smaller compared with that in the reference convergent estuary (Fig. 4c). Apart from the differences in amplitudes, the longitudinal variations of both the astronomical constituent and the overtide and their spatial dependence on river discharge exhibit identical patterns as the reference convergent estuary (Figs. 3 and 4). These consistent results imply that channel convergence does not fundamentally change the spatial dependence of overtide behavior on river discharge; hence, model results on the prismatic channel are examined in depth in this work for simplicity.

Contribution of the Nonlinear Processes

We quantify the individual contribution of different nonlinear terms on M_4 and their variations along the estuary based on the method proposed in the "Theoretical Analysis of Overtide Generation" section and model-produced mean water level height, mean current, and tidal amplitudes. In the absence of river discharge (scenario pQ0), the discharge gradient term is the largest contribution to M_4 overtide generation owing to strong landward damping of M_2 and subsequent longitudinal flux gradients, followed by bottom friction and advection (Fig. 5a). Bottom friction is shown to be more significant than the other terms, when there is a

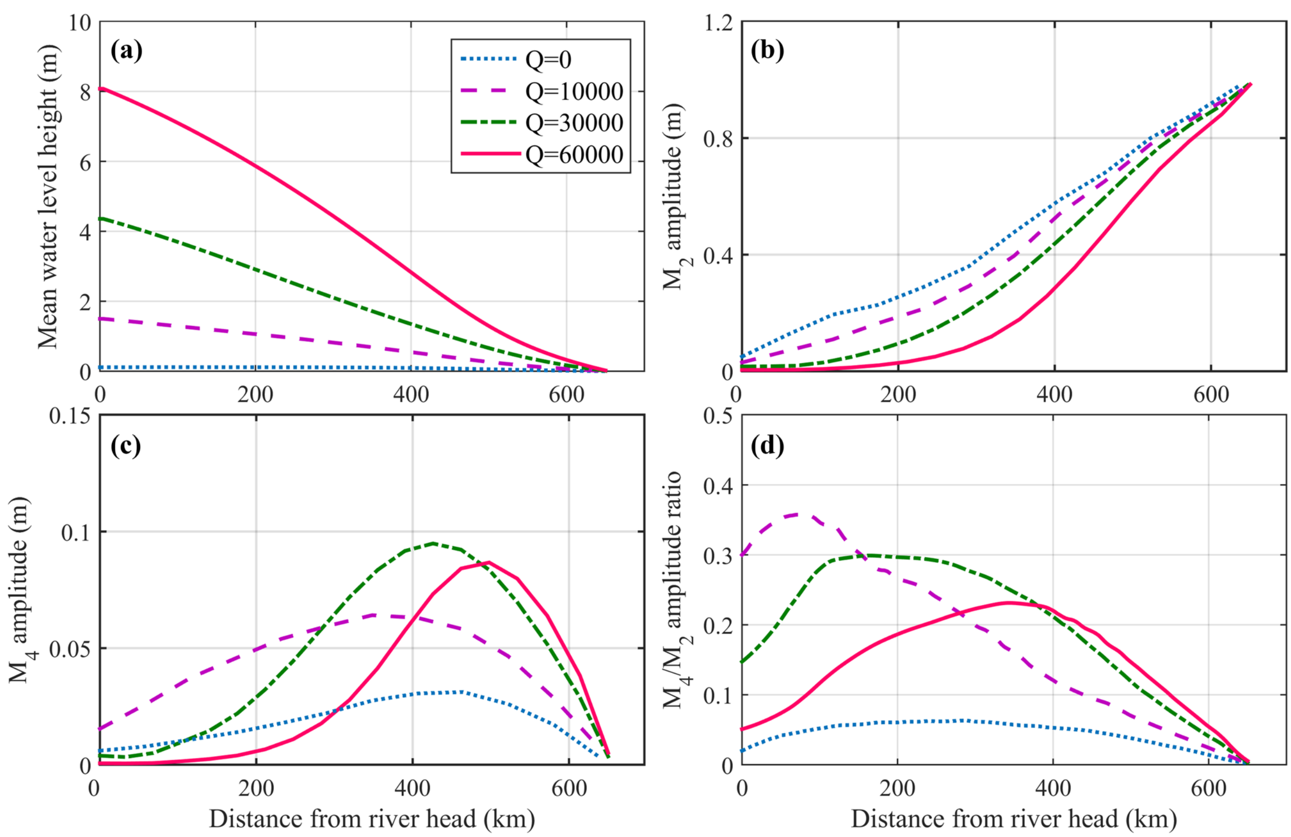

Fig. 4 Model-reproduced longitudinal variations of **a** mean water level height, **b** M_2 tidal amplitude, **c** M_4 tidal amplitude, and **d** the M_4 to M_2 amplitude ratio under different river discharge in the prismatic estuary

river discharge (Fig. 5b-d). The impact of quadratic bottom stress is much more important than that of depth variations. The advection term is of minor importance compared with the other two nonlinear terms.

Spatially, the impact of bottom friction is more profound in the landward regions, whereas the impact of discharge gradient and advection terms is more apparent in the seaward regions close the estuary mouth. The location of maximum M_4 amplitude is close to the peak under the combined contribution of discharge gradient and advection in the pQ0 scenario and to the peak in bottom friction in the other three scenarios. Overall, these results suggest that the bottom friction, or more precisely the quadratic bottom stress, is the dominant forcing in generating M_4 overtide in the circumstances with significant river discharge. Note that the contribution of the bottom friction term is non-negligible in the pQ0 scenario (no river discharge). This is because there is a seaward mean current, i.e., Stokes return flow, which plays a similar a role on the tides as does a river discharge induced mean current; although the magnitude of the Stokes return flow is comparatively small.

The significance of the quadratic bottom stress can be further inferred when comparing model results under quadratic and linear bottom stress. The quadratic bottom stress can be linearized using the first order of the method based on the energy dissipation condition of Lorentz (1926), as that in Zimmerman (1992) and Hibma et al. (2003) (see section II in SI). When similar simulations are run using linear bottom stress, damping of the principal M_2 tide is smaller (see Figure S5). Measurable M_4 tide is still detected inside the estuary under a linear bottom stress, which is ascribed to the effects of the nonlinear advection and depth variation terms, but its amplitude is smaller compared to those under a quadratic bottom stress (Figure S5). Moreover, increasing river discharge neither induces more damping of principal M_2 tide nor more overtide generation under a linear bottom stress. These results and comparison confirm the role of quadratic bottom stress on overtide generation, particularly when river discharge is large.

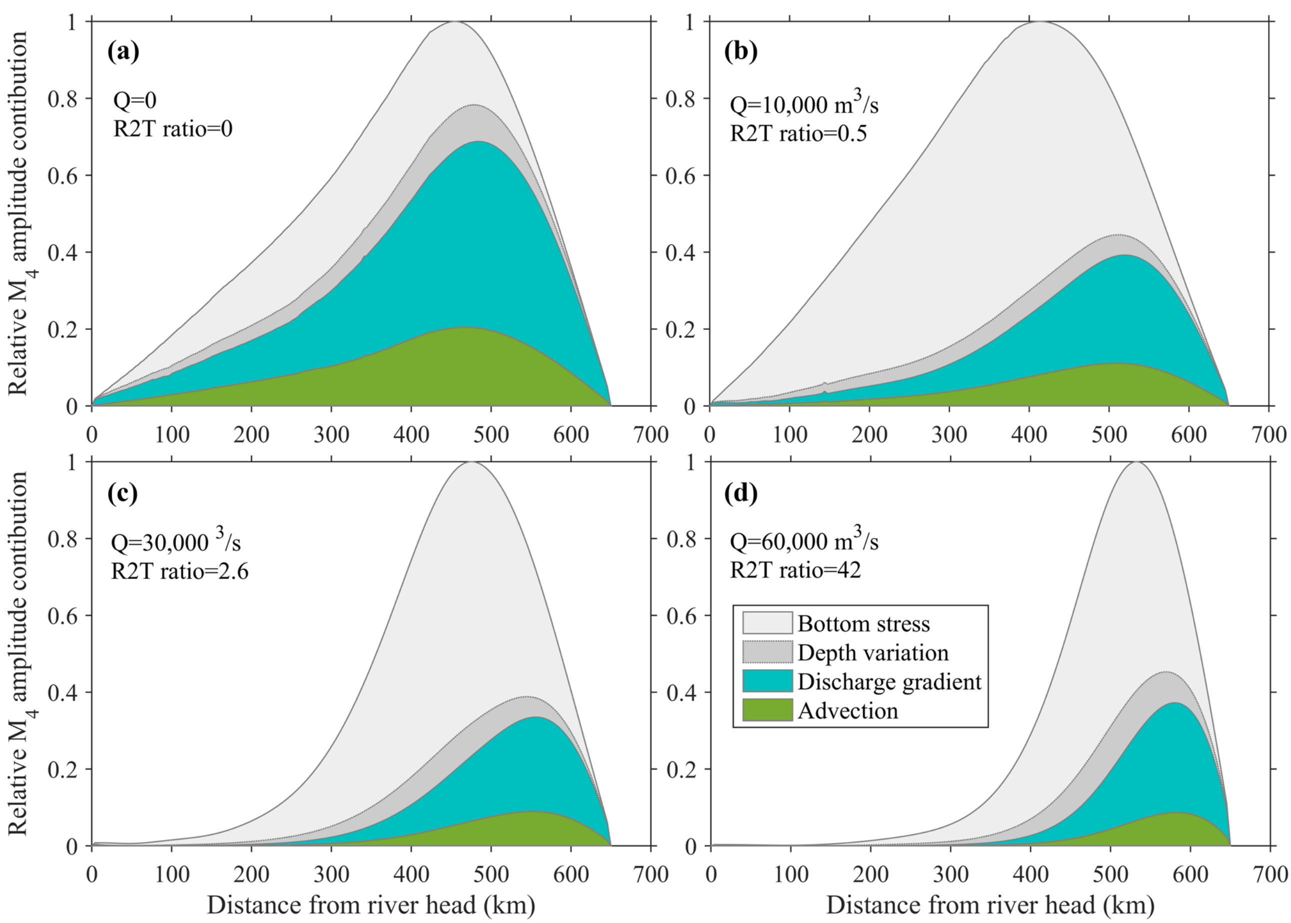

Fig. 5 Quantification of the relative importance of three nonlinear terms (the patch area) on M_4 overtide amplitude in the **a** pQ0, **b** pQ1, **c** pQ3, and **d** pQ6 scenarios in the prismatic channel. The contribution of bottom friction is divided into the components of bottom stress and depth variation. The relative M_4 amplitude is normalized by the maximal value in each scenario

Quantification of the River Discharge Threshold

The model results imply that the M_4 amplitude first increases and then decreases as the astronomical M_2 tide is increasingly dissipated by larger river discharges. It implies the presence of an intermediate condition under which the M_4 tide may reach maximum. To better capture and reveal the intermediate threshold, we run extra simulations considering constant river discharges in the range of 0 to 60,000 m^3/s at an increment of 5000 m^3/s. We then integrate the total (tide-averaged) energy of the M_2 and M_4 tides ($kg \cdot m^2/s^2$) throughout the estuary, according to Eq. 14, to represent accumulated tidal strength. We see that the total energy of the M_2 tide decreases approximately exponentially with increasing R2T ratios (Fig. 6a). The decrease is more significant for $R2T < 5$ (see Figure S3a). When taking the pQ0 scenario as the reference, the ratios of the total energy of M_4 in the scenarios with river discharge to that in the pQ0 scenario, however, first increase with increasing R2T ratio from zero and reach a peak when the R2T ratio is close to unity, followed by a decrease as the R2T ratio further increases (Fig. 6a). The maximal total energy of M_4 is 3.7 times larger than the case with no river discharge in the prismatic estuary (when M_2 is 1.0 m). Similarly, the energy ratios of M_4 to M_2 tides display similar variations as the total energy variation of the M_4 tide, with a peak reached when the R2T ratio is around 1–2 (Fig. 6b).

The results of the sensitivity scenarios under varying degrees of width convergence show similar variations of the total energy ratio of M_4 to M_2 tides with increasing R2T ratios, i.e., increase first, maximum reached, and followed by a decrease (Fig. 6). River-enhanced generation of M_4 increases at a smaller rate under larger M_2 tide, when compared with the pQ0 scenario (Fig. 6a), because tidal dissipation rates are larger under larger tides, thus smaller overtide generation in the scenarios which include river discharge. However, the energy ratios of M_4 to M_2 increase with tidal amplitude (Fig. 6b), suggesting an increasing percentage of M_2 energy is transferred to the overtide. This is because stronger tides benefit river-tide interactions and the consequent generation of overtides. Other than these differences, the change behaviors of the energy ratios with increasing R2T are consistent. Overall, these results consistently imply that a river discharge smaller than an intermediate threshold favors more M_4 tide generation, whereas a larger river discharge above the threshold constrains M_4 tide.

The model results consistently suggest that an intermediate river discharge with a R2T ratio around unity benefits maximal M_4 overtide generation (Fig. 6). While a prismatic estuary is characterized by $R2T = 1$ as an optimum threshold for maximal M_4 generation, convergent estuaries show some variations around unity, i.e., $R2T > 1$ in mildly convergent systems and $R2T < 1$ in strongly convergent systems. The R2T threshold, however, varies in a narrow range in all scenarios in this study, i.e., 0.7–1.2. It confirms the presence of an intermediate threshold in nonlinear overtide changes in response to increasing river discharges.

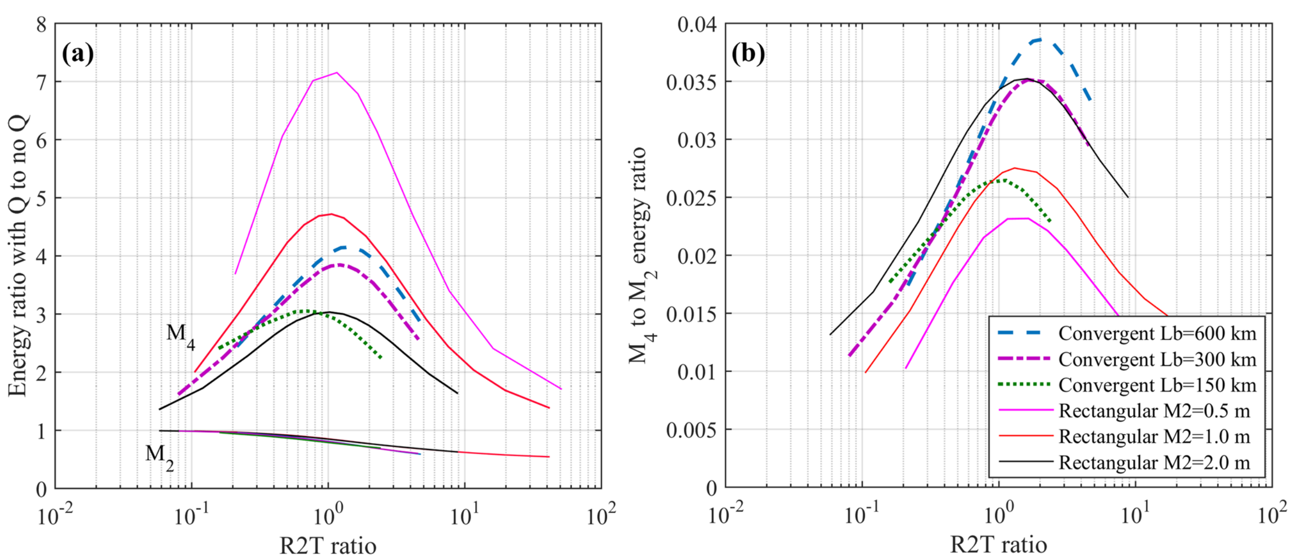

Fig. 6 **a** The ratio of the integrated total energy (TE) in the scenarios with river discharge to the case without river discharge (Q0 scenarios) for both M_2 (thin lines) and M_4 (thick lines) tides, and **b** the ratio of total M_4 tide energy to M_2 tide, as a function of the ratio of river discharge to tide-mean discharge at the estuary mouth (R2T ratio). Also see Figure S3 in the SI

Discussion

Comparison with Actual Estuaries

The modeled overtide variability is consistent with findings in real-world estuaries. The modeled results between the cQ1 and cQ3 scenarios agree with the streamwise variations in the astronomical tides and overtides under low and high river discharges in the Changjiang Estuary. The modeled variation trend of the M_4 to M_2 amplitude ratios in response to increasing river discharge also agrees well with that in the Changjiang Estuary (see Figure S4). In the Amazon Estuary where the river discharge is similarly high and varies over a large range, the M_4 amplitude was larger under a mean river discharge compared to an idealized situation with zero discharge (Fig. 7c; Gallo and Vinzon 2005). This is again consistent with the modeled differences between the cQ0 and cQ1 scenarios in this study. In the Columbia Estuary, a maximum in M_4 amplitude is approached in the seaward parts of the estuary, followed by a subsequent decrease upriver under a yearly mean river discharge (Fig. 7; Jay et al. 2014). The model results also explain why a higher river discharge hastens the high water and delays the low water in the seaward parts of the Saint Lawrence Estuary (Godin 1985, 1999). In the Ganges–Brahmaputra-Meghna Delta, model results suggested enhanced quarter-diurnal tides in the seaward regions of the delta and a transition from increase to decrease in the landward regions with increasing river discharge (Elahi et al. 2020). These field data and model results confirm that the findings regarding the spatial dependence of overtide on river discharge are ubiquitous for estuaries with large river discharges.

The above-mentioned nonlinear overtide changes were predominantly reported in large estuaries and deltas where both river and tidal influences are profound, e.g., the Amazon (Gallo and Vinzon 2005), Changjiang (Guo et al. 2015), and Ganges (Elahi et al. 2020). However, similar phenomenon has not been documented in other tide-dominated estuaries with relatively smaller river discharge, although the importance of overtide in controlling tidal asymmetry and residual transport has been widely reported, e.g., in the Humber Estuary in the UK (Winterwerp 2004) and the Scheldt Estuary in the Netherlands (Wang et al. 2002). This is because river discharge in tide-dominated estuaries is overall small and rarely reaches a magnitude that exceeds R2T = 1. For instance, the R2T is < 0.01

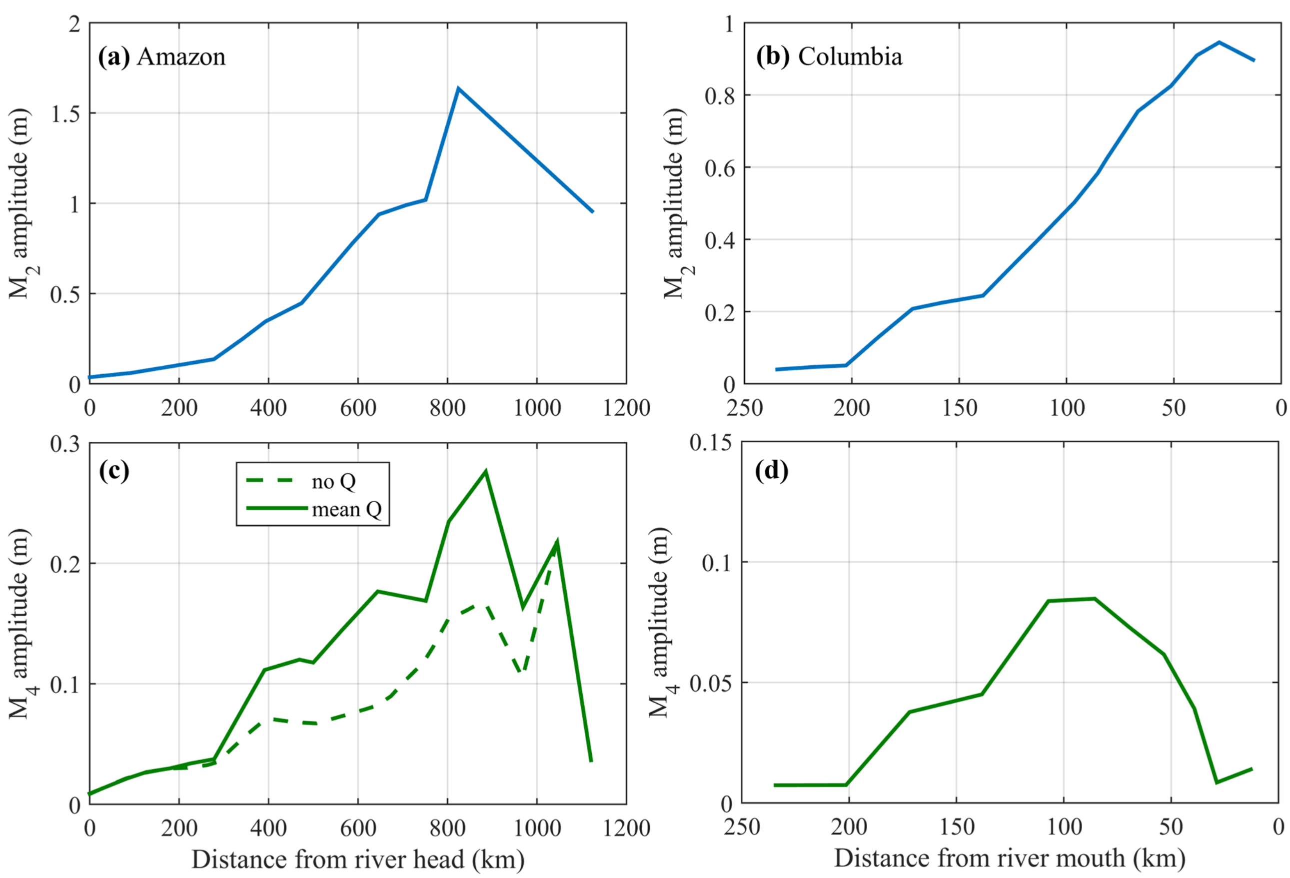

Fig. 7 Amplitude variations of M_2 and M_4 overtide in the **a**, **c** Amazon Estuary and **b**, **d** Columbia Estuary, from Gallo and Vinzon (2005) and Jay et al. (2014), respectively

in the Scheldt Estuary (van Rijn 2011; Wang et al. 2019), and it is ~0.012 in the Humber Estuary (Winterwerp 2004; Townend et al. 2007). Therefore, the role of river discharge in stimulating tidal wave deformation and overtide generation (when R2T < 1) has been widely reported in these tide-dominated estuaries, whereas the situation with R2T > 1 is far less prevalent and hence less documented.

Moreover, most tide-dominated estuaries are relatively shorter in physical length compared with tidal wavelength; hence, the space-dependent overtide variations are less apparent compared with that in large estuaries. Large estuaries with high river discharge are comparatively much longer, in terms of the inland extent of tidal propagation, despite the enhanced tidal damping due to the river discharge. For instance, tidal waves propagate inland ~1100 km in the Amazon Estuary and ~650 km in the Changjiang Estuary. This long distance tidal wave propagation is possible because of the smaller bed level gradients in the low-lying delta plains formed under high river discharge and sediment supply. The large estuaries thus provide space for slower tidal wave damping and facilitate wave deformation to accommodate the large variations of river discharges and friction at different time scales (Zhang et al. 2015).

Role of River Discharge

River discharge has twofold effects on tidal propagation and deformation (Fig. 8). River discharge enlarges the mean currents and the effective friction on the moving flow. On the one hand, this induces more damping of the incoming astronomical tides, i.e., more energy dissipation. On the other hand, the river-enhanced bottom friction reinforces the energy transfer from astronomical tides to overtides, i.e., stimulating overtide generation. As more astronomical tidal energy is dissipated by larger river discharges, which is more profound in the landward parts of estuaries, the energy available for transferring to overtides is also constrained. In addition, the overtides generated in the seaward parts of estuaries propagate landward and are damped by higher discharge in the landward regions. As a result, an intermediate river discharge (when the R2T ratio is close to unity) provides an effective bottom stress that will not dissipate the astronomical tides too much, and at the same time stimulates considerable energy transfer to overtides. The intermediate threshold balance leads to the occurrence of a maximum in overtide energy when integrated over the length of the estuary.

River impact on tidal wave propagation and deformation is spatially variable. River discharge substantially elevates the mean water level in the landward parts of estuaries. The consequent larger water level gradient restricts landward wave propagation (Godin 1985; Cai et al. 2019). In the seaward parts of an estuary where the incident tidal waves are less dissipated, the role of river discharge in reinforcing the effective bottom friction and enhancing overtide generation is more pronounced. In contrast, in the landward parts of an estuary, the role of river discharge in dissipation of astronomical tide is more prominent. These spatially variable dynamics explain the contrasting overtide changes in response to increasing river discharge between the landward and seaward parts (Fig. 8). It confirms that tidal wave deformation maybe one of the degrees-of-freedom of estuaries to maintain a state of minimum work by adjusting tidal wave shapes in response to different river discharges (Zhang et al. 2015).

The twofold river effects on tidal propagation and deformation are coherently related to the nonlinear bottom friction. Past studies have indicated that the effects of river discharge on tidal damping are exerted by a mechanism identical to bottom stress (Horrevoets et al. 2004; Cai et al. 2014). River-tide interaction enhances ebb current velocities and the bottom stress on the flow, which subsequently induces larger tidal damping (Alebregtse and de Swart 2016). Past studies have also suggested that the nonlinear advection term is the main cause of M_4 generation in tide-dominant estuaries, while the nonlinear bottom stress term leads to generation of

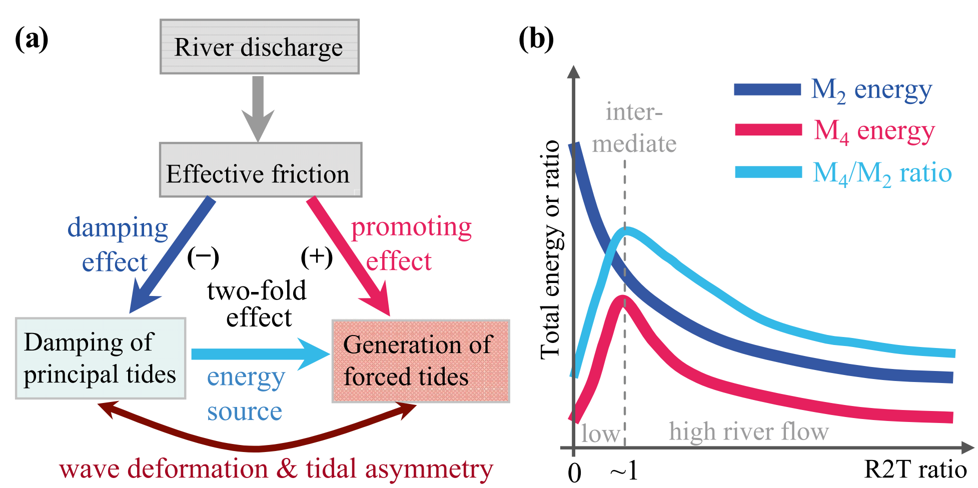

Fig. 8 Sketches showing **a** the twofold effects of river discharge on tidal propagation and deformation through the bottom friction, and **b** the intermediate river discharge threshold that maximizes overtide generation

M_6 (Pingree and Maddock 1978; Parker 1984, 1991; Wang et al. 1999; Elahi et al. 2020). Additionally, the quadratic bottom stress term leads to significant M_4, through river-tide interaction, i.e., between a river-enhanced mean current and M_2 current (Wang et al. 1999). This explains why the M_4 amplitude is larger in the presence of a river discharge and a quadratic bottom stress, compared with the situation with no river discharge and/or a linear bottom stress.

Although the model results are obtained under different but constant river discharges, the findings in this work still hold true when considering time-varying river discharges (see Figures S6-S8 in the SI). One slight difference is that the damping rate of the astronomical tides would be slightly different during the rising and falling limb of a river discharge hydrograph (Sassi and Hoitink 2013), which may be due to a time lag in the influence of river discharge along the length of an estuary.

Implications and Limitations

Better understanding of the overtide changes has broad implications for study of tidal bores, interpretation of extreme high water levels and associated flood risk, tidal asymmetry and tide-averaged sediment transport. Tidal wave deformation changes the height of high water and low water, which then influence flooding risk management, particularly the compound flood risk induced by high river discharge and high tide within estuaries and deltas (Moftakhari et al. 2017). The water level height also affects the water depth for navigational channels. In the extreme situation, tidal wave deformation leads to tidal bores when tides are concurrently amplified and distorted to an extreme degree (Bonneton et al. 2015). Other than the amplification by channel convergence, river discharge is expected to play a role in enhancing wave deformation and tidal bore formations given its dual impacts on tides.

The longitudinally distinct overtide behaviors have implications for spatial division of estuaries (Fig. 9). Traditionally two regions can be identified in the river-to-ocean transition zones, i.e., an inland part dominated by river forcing, with some damped tidal wave influence, unidirectional currents, no salinity, and a seaward part predominantly controlled by tidal forcing, bidirectional currents, and of profound salinity due to saltwater intrusion influence (Jay and Flinchem 1997; Guo et al. 2015, 2020; Fig. 9). Moreover, a larger estuary may be divided into a landward tidal river segment and a

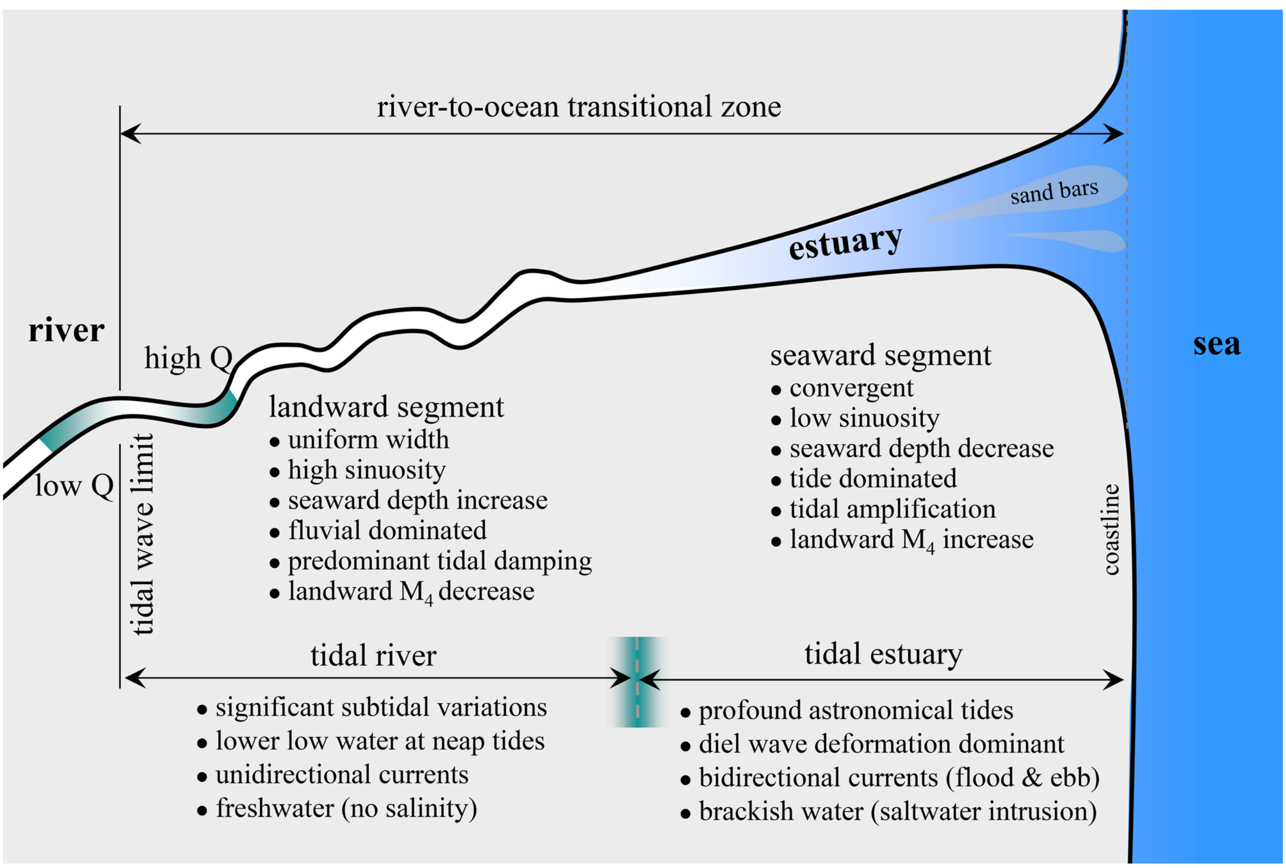

Fig. 9 A conceptual sketch of the river-to-ocean transitional zone with distinctive tidal and hydro-morphological features between a landward tidal river and a seaward tidal estuary segments

seaward tidal estuary segment, based on the relative strength of subtidal signals (Hoitink and Jay 2016) and streamwise hydro-morphological variability (Gugliotta and Saito 2019). Inland tidal river is characterized with lower low water at neap tide than spring tide, sinuous channels with a uniform width, and a seaward increasing water depth, whereas tidal estuary is likely more convergent with a decrease in water depth in the seaward direction and affected by saltwater intrusion (Guo et al. 2015; Hoitink and Jay 2016; Gugliotta and Saito 2019). In this work focusing on overtide, the seaward part of an estuary is identified as the region with a landward increase in overtide amplitude, while the landward part is featured by a landward decrease in overtide amplitude (Fig. 9). The location of the division is at the point of maximal overtide amplitude, and its position moves with river discharge. Note that this division tends to be more seaward compared with the transition between tidal river and tidal estuary.

Knowledge of the nonlinear overtide changes informs study of the overtide components of tidal currents and associated sediment transport processes. The interactions between mean currents and the quarter-diurnal overtide currents contribute to net water transport (Alebregtse and de Swart 2016). The current interactions between M_2 and M_4 tides play a profound role in controlling tidally averaged sediment transport, e.g., sediment import or export and resultant infilling or empty of estuaries, particularly when river discharge is small (Postma 1961; Guo et al. 2014). Largest seaward sediment flushing and development of deepest estuarine equilibrium bed profile occurs when the river-controlled mean current velocity is equal to tide-induced current velocity (Guo et al. 2014). It is because river-tide interactions enhance seaward residual sediment transport, while a much larger river discharge would dampen the effect of river-tide interaction and tidal asymmetry.

Although channel convergence is not modeled to fundamentally change the overtide variations in response to varying river discharges, the potential impact of the simplified model setting in this study still mandates careful evaluation. For instance, regional narrowing and shallowness in geometry and morphology will induce variations in tidal damping rates and distribution of amplitudes. The bed profile condition used in the model affects tidal propagation and hence the location of maximal M_4 amplitude. River estuaries can be partially or highly stratified, and a density difference and associated stratification affect tides by reducing the effective drag coefficient and changing the pressure-gradient term (Talke and Jay 2020). This impact maybe further manifested in surface amplitude of overtide given the role of river-tide current interactions in the nonlinear terms (Dijkstra et al. 2017). Intertidal flats are known as a sink of momentum and would exert additional impact on tidal wave propagation (Hepkema et al. 2018). Exclusion of intertidal flats in this work thus may lead to overestimation of the overtide amplitude. Furthermore, the intermediate river discharge threshold is expected to vary with estuarine size and shape, given that tidal mean discharge is strongly affected by estuarine morphology. Barrier dams within tidal wave propagation limit, e.g., the Bonneville Dam in the lower Columbia River (Jay et al. 2014), may induce wave reflection that affects tidal wave dynamics, in contrasts to the unconstrained estuaries. These dynamic complexities merit site-specific examination.

Conclusions

This work is devoted to examining overtide behavior under varying river discharges in long and friction-dominated estuaries. Inspired by preliminary findings in the Changjiang Estuary, we use a numerical model for a schematized estuary to capture the nonlinear tidal dynamics under varying river discharges. Model results reveal significant overtide M_4 generated inside the estuary and its amplitude exhibits strong spatial dependence and nonlinear changes. While the astronomical M_2 tide is increasingly dissipated as the R2T ratio increases from zero, the M_4 amplitude decreases in the landward parts of the estuary but increases in the seaward parts. With increasing R2T ratio, the total energy of M_4 overtide integrated throughout the estuary first increases and reaches a peak when the R2T ratio is close to unity, followed by a decrease when river discharge further increases. The modeled nonlinear overtide changes are quantitatively validated by data in the Changjiang and Amazon Estuaries.

Sensitivity simulations confirm the dominant role of river-enhanced bottom friction in controlling the overtide behavior. The enhanced bottom friction has twofold effects on tidal wave propagation and deformation, namely dissipation of astronomical tidal energy and stimulation of energy transfer to overtides. As a result, an intermediate river discharge threshold benefits maximal overtide generation. This study demonstrates the need to look at both tidal wave propagation and deformation at the same time in examination of tidal wave dynamics, as well as their nonlinear spatial variations in large river estuaries. The findings have implications for studies of tidal bores and tidal asymmetry and associated morphological changes in large estuaries.

Supplementary Information The online version contains supplementary material available at https://doi.org/10.1007/s12237-023-01183-0.

Funding This work is supported by National Natural Science Foundation of China (Nos. U2040216; 41876091), and partially sponsored by the project "Coping with deltas in transition" within the Programme of Strategic Scientific Alliance between China and The Netherlands (PSA), financed by the Ministry of Science and Technology, P.R. China (MOST) (No. 2016YFE0133700) and Royal Netherlands Academy of Arts and Sciences (KNAW) (No. PSA-SA-E-02).

Data Availability Data are available upon resquest of the corresponding author.

References

Alebregtse, N.C., and H.E. de Swart. 2016. Effect of river discharge and geometry on tides and net water transport in an estuarine network, an idealized model applied to the Yangtze Estuary. *Continental Shelf Research* 123: 29–49.

Bonneton, P., N. Bonneton, J.-P. Parisot, and B. Castelle. 2015. Tidal bore dynamics in funnel-shaped estuaries. *Journal of Geophysical Research: Oceans* 120: 923–941.

Bloomfield, P. 2013. *Fourier analysis of time series: An introduction (2nd), Wiley Series in Probability and Statistics*. New York: John Wiley & Sons.

Cai, H.Y., H.H.G. Savenije, and M. Toffolon. 2014. Linking the river to the estuary: Influence of river discharge on tidal damping. *Hydrology and Earth System Science* 18: 287–304.

Cai, H.Y., H.H.G. Savenije, E. Garel, X.Y. Zhang, L.C. Guo, M. Zhang, F. Liu, and Q.S. Yang. 2019. Seasonal behaviors of tidal damping and residual water level slope in the Yangtze River estuary: Identifying the critical position and river discharge for maximum tidal damping. *Hydrology Earth System Science* 23: 2779–2794.

Chernetsky, A.S., H.M. Schuttelaars, and S.A. Talke. 2010. The effect of tidal asymmetry and temporal settling lag on sediment trapping in tidal estuaries. *Ocean Dynamics* 60: 1219–1241.

Dijkstra, Y.M., R.L. Brouwer, H.M. Schuttelaars, and G.P. Schramkowski. 2017. The iFlow modelling framework v2.4: A modular idealized process-based model for flow and transport in estuaries. *Geoscientific Model Development* 10: 2691–2731.

Dronkers, J.J. 1964. *Tidal computations in rivers and coastal waters*, 219–304. Amsterdam: North-Holland.

Elahi, M.W.E., I. Jalón-Rojas, X.H. Wang, and E.A. Ritchie. 2020. Influence of seasonal river discharge on tidal propagation in the Ganges-Brahmaputra-Meghna Delta, Bangladesh. *Journal of Geophysical Research: Oceans* 125: 1–19.

Friedrichs, C.T., and D.G. Aubrey. 1988. Non-linear tidal distortion in shallow well-mixed estuaries: A synthesis. *Estuarine, Coastal and Shelf Science* 27: 521–545.

Friedrichs, C.T., and D.G. Aubrey. 1994. Tidal propagation in strongly convergent channels. *Journal of Geophysical Research* 99: 3321–3336.

Gallo, M.N., and S.B. Vinzon. 2005. Generation of overtides and compound tides in the Amazon Estuary. *Ocean Dynamics* 55: 441–448.

Godin, G. 1985. Modification of river tides by the discharge. *Journal of Waterway, Port, Coastal and Ocean Engineering* 111 (2): 257–274.

Godin, G. 1991. Frictional effects in river tides. In *Tidal hydrodynamics*, ed. B.B. Parker, 379–402. Toronto: John Wiley.

Godin, G. 1999. The propagation of tides up rivers with special consideration of the upper Saint Lawrence River. *Estuarine, Coastal and Shelf Science* 48: 307–324.

Godin, G., and A. Martinez. 1994. Numerical experiment to investigate the effect of quadratic friction on the propagation of tides in a channel. *Continental Shelf Research* 14: 723–748.

Green, G. 1837. On the motion of waves in a variable canal of small depth and width. *Transactions of the Cambridge Philosophical Society* 6:457– 462.

Gugliotta, M., and Y. Saito. 2019. Matching trends in channel width, sinuosity, and depth along the fluvial to marine transition zone of tide-dominated river deltas: The needs for a revision of depositional and hydraulic models. *Earth-Science Reviews* 191: 93–113.

Guo, L.C., N. Su, C.Y. Zhu, and Q. He. 2018. How have the river discharges and sediment loads changed in the Changjiang River basin downstream of the Three Gorges Dam? *Journal of Hydrology* 560: 259–274.

Guo, L.C., M. van der Wegen, D.A. Jay, P. Matte, Z.B. Wang, J.A. Roelvink, and Q. He. 2015. River-tide dynamics: exploration of nonstationary and nonlinear tidal behavior in the Yangtze River estuary. *Journal of Geophysical Research: Oceans* 120. https://doi.org/10.1002/2014JC010491.

Guo L.C., M. van der Wegen, D. Roelvink, and Q. He. 2014. The role of river flow and tidal asymmetry on 1D estuarine morphodynamics. *Journal of Geophysical Research: Earth Surface* 119: 2315–2334.

Guo, L.C., M. van der Wegen, Z.B. Wang, J.A. Roelvink, and Q. He. 2016. Exploring the impacts of multiple tidal constituents and varying river flow on long-term, large scale estuarine morphodynamics by means of a 1D model. *Journal of Geophysical Research: Earth Surface* 120. https://doi.org/10.1002/2016JF003821.

Guo, L.C., Z.B. Wang, I. Townend, and Q. He. 2019. Quantification of tidal asymmetry in varying tidal environments. *Journal of Geophysical Research: Oceans* 124: 773–787.

Guo, L.C., C.Y. Zhu, X.F. Wu, Y.Y. Wang, D.A. Jay, I. Townend, Z.B. Wang, and Q. He. 2020. Strong inland propagation of low-frequency long waves in river estuaries. *Geophysical Research Letters* 47: e2020GL089112. https://doi.org/10.1029/2020GL089112.

Hepkema, T.M., H.E. de Swart, A. Zagaris, and M. Duran-Matute. 2018. Sensitivity of tidal characteristics in double inlet systems to momentum dissipation on tidal flats: A perturbation analysis. *Ocean Dynamics* 68: 439–455.

Hibma, A., H.M. Schuttelaars, and Z.B. Wang. 2003. Comparison of longitudinal equilibrium profiles of estuaries in idealized and process-based models. *Ocean Dynamics* 53: 252–269.

Hoitink, A.J.F., and D.A. Jay. 2016. Tidal river dynamics: Implications for deltas. *Reviews of Geophysics* 54: 240–272.

Horrevoets, A.C., H.H.G. Savenije, J.N. Schuurman, and S. Graas. 2004. The influence of river discharge on tidal damping in alluvial estuaries. *Journal of Hydrology* 294: 213–228.

Jay, D.A. 1991. Green's law revisited: Tidal long-wave propagation in channels with strong topography. *Journal of Geophysical Research* 96: 20585–20598.

Jay, D.A., and E.P. Flinchem. 1997. Interaction of fluctuating river flow with a barotropic tide: a demonstration of wavelet tidal analysis methods. *Journal of Geophysical Research* 102(C3): 5705–5720.

Jay D.A., K. Leffler, H.L. Diefenderfer, and A.B. Borde. 2014. Tidal-fluvial and estuarine processes in the lower Columbia River: I. along-channel water level variations, Pacific Ocean to Bonneville Dam. *Estuaries and Coasts*. https://doi.org/10.1007/s12237-014-9819-0.

Kästner, K., A.J.F. Hoitink, P.J.J.F. Torfs, E. Deleersnijder, and N.S. Ningsih. 2019. Propgation of tides along a river with a sloping bed. *Journal of Fluid Mechanics* 872: 39–73.

Kreiss, H. 1957. Some remarks about nonlinear oscillations in tidal channels. *Tellus* 9: 53–68.

Lanzoni, S., and G. Seminara. 1998. On tide propagation in convergent estuaries. *Journal of Geophysical Research* 103 (C13): 30793–30812.

Lanzoni, S., and A. D'Alpaos. 2015. On funneling of tidal channels. *Journal of Geophysical Research: Earth Surface* 120: 433–452.

Le Provost, C. 1991. Generation of overtides and compound tides (review). In *Tidal Hydrodynamics*, ed. B.B. Parker, 269–295. Toronto: John Wiley.

Lesser G.R., J.A. Roelvink, J.A.T.M. van Kester, and G.S. Stelling. 2004. Development and validation of a three dimensional morphological model. *Coastal Engineering* 51: 883–915.

Lieberthal, B., K. Huguenard, L. Ross, and K. Bears. 2019. The generation of overtides in flow around a headland in a low inflow estuary. *Journal of Geophysical Research: Oceans* 124: 955–980.

Lorentz, H.A. 1926. Report State Committee Zuiderzee (in Dutch).
Losada, M.A., M. Diez-Minguito, and M.A. Reyes-Merlo. 2017. Tidal-fluvial interaction in the Guadalquivir River Estuary: Spatial and frequency-dependent response of currents and water levels. *Journal of Geophysical Research: Oceans* 122: 847–865.
Lu, S., C.F. Tong, D.-Y. Lee, J.H. Zheng, J. Shen, W. Zhang, and Y.X. Yan. 2015. Propagation of tidal waves up in the Yangtze Estuary during the dry season. *Journal of Geophysical Research: Oceans* 120: 6445–6473.
Moftakhari, H., G. Salvadori, A. AghaKouchak, B. Sanders, and R. Matthew. 2017. Compounding effects of sea level rise and fluvial flooding. *Proceedings of the National Academy of Sciences* 114 (37): 9785–9790.
Nidzieko, N.J. 2010. Tidal asymmetry in estuaries with mixed semidiurnal/diurnal tides. *Journal of Geophysical Research: Oceans* 115: C08006. https://doi.org/10.1029/2009JC005864.
Parker, B.B. 1984. Frictional effects on tidal dynamics of shallow estuary. PhD. Dissertation, The Johns Hopkins University, 291 pp.
Parker, B.B. 1991. The relative importance of the various nonlinear mechanisms in a wide range of tidal interactions. In *Tidal Hydrodynamics*, ed. B.B. Parker, 237–268. New York: John Wiley.
Pawlowicz, R., B. Beardsley, and S. Lentz. 2002. Classical tidal harmonic analysis including error estimates in MATLAB using T_TIDE. *Computers & Geosciences* 28: 929–937.
Pingree, R.D., and L. Maddock. 1978. The M_4 tide in the English Channel derived from a non-linear numerical model of the M_2 tide. *Deep-Sea Research* 25: 52–63.
Proudman, J. 1953. Dynamical Oceanography. Wiley, New York, 409 pp.
Postma, H. 1961. Transport and accumulation of suspended matter in the Dutch Wadden Sea. *Netherlands Journal of Sea Research* 1: 148–190.
Pugh, D.T. 1987. Tides, surges and mean sea-level, 472 pp., John Wiley, Hoboken, N.J.
Ridderinkhof, W., H.E. de Swart, M. van der Vegt, N.C. Alebregtse, and P. Hoekstra. 2014. Geometry of tidal inlet systems: A key factor for the net sediment transport in tidal inlets. *Journal of Geophysical Research: Oceans* 119 (10): 6988–7006. https://doi.org/10.1002/2014jc010226.
Sassi, M.G., and A.J.F. Hoitink. 2013. River flow controls on tides and tide-mean water level profiles in a tidal freshwater river. *Journal of Geophysical Research* 118: 1–3. https://doi.org/10.1002/jgrc.20297.
Savenije, H.H.G. 2005. Salinity and tides in alluvial estuaries. Elsevier Science, Amsterdam.
Speer P.E., and D.G. Aubrey. 1985. A study of non-linear tidal propagation in shallow inlet/estuarine systems Part II: theory. Estuarine. *Coastal and Shelf Science* 21: 207–224.
Stronach, J.A., and T.S. Murty. 1989. Nonlinear river-tidal interactions in the Fraser River. *Canada. Marine Geodesy* 13 (4): 313–339.
Talke S.A., and D.A. Jay. 2020. Changing tides: the role of natural and anthropogenic factors. *Annual Review of Marine Sciences* 12: 14.1–14.31.
Toffolon, M., and H.H.G. Savenije. 2011. Revisiting linearized one-dimensional tidal propagation. *Journal of Geophysical Research* 116, C07007. https://doi.org/10.1029/2010JC006616.
Townend, I.H., Z.B. Wang, and J.G. Rees. 2007. Millennial to annual volume changes in the Humber Estuary. *Proceedings of the Royal Society A*. https://doi.org/10.1098/rspa.2006.1798.
van Rijn, L.C. 2011. Analytical and numerical analysis of tides and salinities in estuaries, part I: Tidal wave propagation in convergent estuaries. *Ocean Dynamics* 61: 1719–1741.
Walters, R.A., and R.E. Werner. 1991. Nonlinear generation of overtide, compound tides, and residuals. In *Tidal hydrodynamics*, ed. B.B. Parker, 297–320. Toronto: John Wiley.
Wang Z.B., H. Juken, and H.J. de Vriend. 1999. Tidal asymmetry and residual sediment transport in estuaries. WL|Hydraulic, report No. Z2749, 66 pp.
Wang, Z.B., M. Jeuken, H. Gerritsen, H.J. de Vriend, and B.A. Kornman. 2002. Morphology and asymmetry of vertical tides in the Westerschelde estuary. *Continental Shelf Research* 22: 2599–2609.
Wang, Z.B., W. Vandenbruwaene, M. Taal, and H. Winterwerp. 2019. Amplification and deformation of tidal wave in the Upper Scheldt Estuary. *Ocean Dynamics*. https://doi.org/10.1007/s10236-019-01281-3.
Winterwerp, J.C. 2004. The transport of fine sediment in shallow basins: Humber case study. Delft Hydraulics Report No. Z3506, 76pp.
Zimmerman, J.T.F. 1992. On the Lorentz linearization of a nonlinearly damped tidal Helmholtz oscillator. *Proceeding KNAW* 95 (1): 127–145.
Zhang, M., I. Townend, H.Y. Cai, and Y.X. Zhou. 2015. Seasonal variation of tidal prism and energy in the Changjiang River estuary: A numerical study. *Chinese Journal of Oceanology and Limnology* 33 (5): 1–12.

Authors and Affiliations

Leicheng Guo[1] · Chunyan Zhu[1] · Huayang Cai[2] · Zheng Bing Wang[3,4] · Ian Townend[5] · Qing He[1]

[1] State Key Lab of Estuarine and Coastal Research, East China Normal University, Shanghai 200241, China

[2] School of Ocean Engineering and Technology, Sun Yat-Sen University, Guangzhou 510275, China

[3] Department of Hydraulic Engineering, Faculty of Civil Engineering and Geosciences, Delft University of Technology, Delft 2600GA, The Netherlands

[4] Marine and Coastal Systems Department, Deltares, Delft 2629 HV, The Netherlands

[5] School of Ocean and Earth Sciences, University of Southampton, Southampton, UK